Nanoscale mechanical and electrical characterization of the interphase in polyimide/silicon nitride nanocomposites

Mohammed Houssat, Christina Villeneuve-Faure, Nadine Lahoud Dignat, Jean-Pascal Cambronne

IOP Publishing Journal Title
Journal **XX** (XXXX) XXXXXX https://doi.org/XXXX/XXXX

Nanoscale mechanical and electrical characterization of the interphase in polyimide/silicon nitride nanocomposites

Mohammed Houssat, Christina Villeneuve-Faure, Nadine Lahoud Dignat and Jean-Pascal Cambronne

LAPLACE, Université de Toulouse, CNRS, INPT, UPS, Toulouse, France

E-mail: villeneuve@laplace.univ-tlse.fr
lahoud@laplace.univ-tlse.fr

Received xxxxxx
Accepted for publication xxxxxx
Published xxxxxx

Abstract

Polymer nanocomposites (pNC) have attracted wide interests in electrical insulation applications. Compared to neat matrices or microcomposites, pNC provide significant improvements in combined electrical, mechanical and thermal properties. In the understanding of the reasons behind these improvements, a major role was attributed to the interphase, the interaction zone between the nanoparticles (NP) and the matrix. Because of their nanoscale dimensions, the interphase properties are mostly theoretically described but rarely experimentally characterized. The aim of this study is to propose a nanoscale measurement protocol in order to probe mechanical (Young modulus) and electrical (dielectric permittivity) interphase features using, respectively, the peak force quantitative nanomechanical (PF-QNM) and the electrostatic force microscopy (EFM) modes of the atomic force microscopy. Measurements are performed on polyimide (PI)/silicon nitride (Si_3N_4) nanocomposite and the effect of a silane coupling agent treatment of Si_3N_4 NP is considered. In order to accurately probe mechanical properties in PF-QNM mode, the impacting parameters such as the applied force, the deformation and the topography are taken into account. The interphase region has shown a higher elastic modulus compared to the matrix and a higher width (W_I) value for treated NP. From EFM measurements combined to a finite element model feeded with the W_I values obtained from PF-QNM, the interphase permittivity is determined. The corresponding values are lower than the matrix one and similar for untreated and treated NP. This is in total agreement with its higher elastic modulus and implies that the interphase is a region around the NP where the polymer chains present a better organization and thus, a restricted mobility.

Keywords: polymer nanocomposites, interphase, nanoscale characterization, PF-QNM, EFM

1. Introduction

Polymer dielectric materials are broadly used for electrical insulation in a wide range of applications from microelectronic devices [1] to electrical machines [2] and HVDC cables [3]. Within these applications, the polymer insulation undergoes multiple stress conditions leading to its ageing, degradation and failure [4]. Space charge build-up, tree growth and charge injection in HVDC cables [3] or partial discharges in electrical machines [2] as well as high temperature operating conditions in novel wide bandgap semiconductor devices [1] are examples of processes leading to the polymeric insulation breakdown. In this context, the idea of using polymer nanocomposites (pNC), also called nanodielectrics, in electrical insulation was first proposed by Lewis in 1994 [5]. PNC are defined as composites in which nanometric fillers (i.e. at least one of their dimensions in the nanometer range) are dispersed in polymer matrix by several weight percentages (wt%) [6]. With the benefit of having a large surface area, nanometric fillers have also proved their efficacy over micrometric fillers [7-10]. Results have shown that microcomposites improve one of the electrical insulation characteristics at the cost of another, whereas pNC improve the overall characteristics.

A literature review emphasizes that the addition of a small amount of nanofillers (< 10 wt%) in a polymeric matrix improves a lot of macroscopic properties as the breakdown strength, the amount of injected charges, the resistance to partial discharges, the thermal conductivity and the mechanical features [8, 9, 11-14]. This improvement is observed for various nanofillers [15] such as metallic [16], dielectric [17, 18] nanoparticles (NP), graphene [19] and carbon nanotubes (CNT) [20]. Moreover, recent studies have shown the effect of the nanofillers functionalization on final nanodielectric properties. Indeed, the NP surface treatment using a coupling agent reduces the presence of aggregates and affects considerably the dielectric and mechanical performances [21]. Particularly, a considerable improvement of the breakdown strength [22] and a reduction of dielectric losses [23, 24] have been revealed.

In order to explain the nanofiller influence on pNC properties, Lewis has proposed a hypothesis that a transition area named “interphase” is created between the nanofiller and the polymeric matrix [5]. The interphase properties are supposed to strongly influence pNC. Up to this time, a lot of models have been proposed to describe the interphase nanostructure and its properties. The Lewis model describes the interphase as a transition area for one or more properties with charge layer following the Stern/Gouy-Chapman model [5]. The multicore model proposed by Tanaka *et al* describes the interphase as the superposition of three layers and a charge distribution [25]. The first layer of few nanometers thick represents the hard core, the second layer of about 10 nm thick presents a morphological regularity and the third layer of several tens of nm thick is called the loose layer and has a chain conformation different from the polymer matrix. According to the interphase volume model proposed by Raetzke *et al*, the interphase consists of polymer chains with a different morphology than the remaining uninfluenced matrix, due to the bindings and interactions between the filler particle surface and the polymer [26]. This model predicts an interphase thickness around few tens of nm. The Todd-Shii model defines the interphase as a region with different dielectric properties than both matrix and nanofillers [27]. From these models, the interphase thickness is estimated from few nanometers [28, 29] to few hundred of nanometers [30, 31] and the interphase permittivity appears to be less than the matrix one for lot of fillers [32]. However, these models failed to reproduce all experimental results. This is mainly due to the fact that they are based on too strong hypotheses (monodispersed nanofillers, spherical NP, equidistant fillers…). Some attempts were done to adapt these models to the real sample geometry. For example, Pandey *et al* has corrected the Raetzke model to take into account the fillers aggregation but did not manage to explain all macroscale properties [31]. This is probably due to the fact that macroscopic characterization techniques are used to validate a model describing the behavior at a nanoscale.

To overcome this drawback and determine interphase properties at the nanoscale, methods derived from atomic force microscopy (AFM) were more and more used during the past decade. The interphase thickness was probed using mechanical properties modification in tapping (phase images) [33, 34], torsional harmonic AFM indentation [35], peak force quantitative nanomechanical (PF-QNM) [36-38] or electrostatic force microscopy (EFM) [39] modes. However, these studies on the interphase dimension measurements did not provide a robust and optimized

methodology to probe it. The interphase permittivity could be probed at the local scale using EFM [39, 40]. As demonstrated by Gupta *et al* [41], using machine learning and modelled sample, EFM could determine the interphase dielectric permittivity even if the in-depth localization remains unknown but the detection sensitivity decreases when NP are far from the surface [42]. However, for real pNC materials some assumptions about the interphase thickness are needed to deduce the interphase dielectric permittivity [42] which appears less than the matrix one [43]. Moreover, the existence of a charge layer in the interphase area was demonstrated using EFM [44], intermodulation EFM (Im-EFM) [45] and Kelvin probe force microscopy (KPFM) [46]. The interphase polarization was detected in ferroelectric pNC using KPFM [47]. This litterature overview shows that the complete charaterization of interphase properties in real pNC remains challenging. For example, an attempt was made to determine the interphase width and dielectric permittivity from the same EFM phase shift measurement for epoxy/$BaTiO_3$ pNC [39, 44]. However, the spatial resolution degradation of the EFM was not taken into account even when the bump height and the lift were obviously high.

The aim of this study is to characterize the interphase mechanical (Young modulus) and electrical (dielectric permittivity) properties, in a real pNC material, using PF-QNM and EFM measurements. A systematic approach is proposed for each technique in order to improve the understanding of physical mechanisms occurring during measurements and to propose an optimized methodology for a strict charaterization of interphase properties. To reach this goal polyimide (PI)/silicon nitride (Si_3N_4) pNC will be investigated. Indeed, PI is largely used in electrical insulation applications due to its high resistivity, high glass transition temperature, high thermal stabililty, low dielectric constant, high breakdown field, inertness to solvent and easy processing [1, 48]. However, the PI properties are modified at high temperatures showing a degradation of its electrical resistivity, dielectric properties and failure field [49-51]. In order to enhance PI properties particularly at high temperatures, the inorganic NP addition to the matrix has shown interesting results [52-54]. Inorganic NP, as Si_3N_4, with high electrical resistivity and high thermal conductivity seem to be extremely advantageous because they allow the insulating material to have a higher thermal conductivity and thus, a better heat dissipation. Moreover, the Si_3N_4 NP functionalization using (3-Aminopropyl) triethoxysilane (APTES) will be used in order to improve the nanofillers dispersion and to modify the interphase thickness and/or properties. Indeed, as the nanofillers surface functionalization could improve the nanodielectric properties, this treatment is supposed to modify the interphase features [10, 21, 23, 55, 56].

2. Materials and methods

2.1 Materials

The PI host matrix is a commercial PI2600 series product purchased from HD microsystems based on biphenyltetracarboxilic dianhydride and p–phenylene diamine precursor monomers (BPDA-PDA). These precursors are dissolved in N-methyl-2-pyrrolidone (NMP) based solvent in order to form a liquid polyamic acid (PAA). After annealing, the obtained PI has a volumetric mass density of 1.48 g cm^{-3}. The Si_3N_4 is provided as spherical amorphous NP (with a volumetric mass density of 2.67 g cm^{-3} and a diameter of 20 to 40 nm) by SkySpring Nanomaterials Inc. The NP surface functionalization is obtained by using APTES (98%) purchased from Sigma-Aldrich.

2.2 Sample preparation

The pNC fabrication process, detailed in [37], is composed of four steps. (i) A 1 % wt / wt solution was prepared by mixing 0.05 g of Si_3N_4 NP with 5 g of the PAA solution for 15 min in order to obtain a homogenous mixture. Another solution was prepared with the addition of a silane coupling agent in order to obtain a NP treated sample. (ii) An ultra-sonication process (70 °C and 300 W) for 1 h (cycles of 2 s ON and 12 s OFF) was used to reduce the size of agglomerates formed during the mechanical dispersion. Then, to get rid of residual aggregates, centrifugal decantation by micro centrifuge (Pico21) was used. PAA/Si_3N_4 solutions were placed in 3 mL tubes before being subjected to 21 000 G (14 400 rpm) centrifugal force for 25 min. Only the supernatant mixture was used (1 mL).

(iii) The nanocomposite (NC) solution was spin-coated for 30 s (3000 rpm) to obtain a thin film with controlled thickness. (iv) The obtained PAA/ Si_3N_4 NC thin film was placed on a hot plate for an annealing in air at 100 °C for 1 min and 175 °C for 3 min. Finally, in order to obtain PI from PAA by the imidization process, the thin film was thermally cured in a SPX Blue-M convection oven in nitrogen atmosphere. Simultaneously, pure PI films were elaborated with the spin coating of the PAA solution followed by the final step annealing treatment.

The pNC layers thickness was probed using KLA-Tencor mechanical profilometer. A thickness of 2.3 µm and 3.4 µm were found for samples with untreated and treated NP respectively. The neat PI films thickness is around 5.8 µm.

2.3 *Interphase nanoscale measurements*

Transmission electron microscopy (TEM) was used to visualize the NP shape and their dispersion into the pNC. A comparison between samples with untreated and treated NP was done showing the functionalization effect on the NP dispersion. These measurements were done using a JEOL JSM 2100F -200 kV apparatus.

AFM measurements were performed using a Bruker Multimode 8 apparatus. Two derived modes, the PF-QNM and the EFM, were used to probe topography, mechanical and electrical properties of the pNC material surface.

Surface topography and mechanical properties of PI/Si_3N_4 pNC were assessed in PF-QNM mode [57] using TAP525 tip. This tip was used as its spring constant is suitable to PI Young modulus which is around 8.5 GPa [58]. For Young modulus quantitative measurement, a three steps calibration method was applied [59]. (i) Static and dynamic deflection sensitivities were determined using force distance curve and scanning mode respectively on hard sapphire sample. (ii) Tip spring constant k was determined using the Sader method [60]. To reach this goal, tip parameters were experimentally determined using the JEOL JSM-6060LV scanning electron microscope (SEM). (iii) Tip radius was calibrated over polystyrene (PS) reference sample whose mechanical properties are close to PI ones (i.e. 2.7 GPa for PS Young modulus), using a deformation target between 2 nm and 4 nm. The measurements were done using 384 x 384 digital pixel resolution, which corresponds to a pixel size of 5.2 nm for 2 µm x 2 µm image size.

As emphasized by Dokulkin *et al*, the extraction of Young modulus map is challenging and is impacted by several parameters as the unpredicted factors of a real tip-sample contact on reference polymer surfaces [61, 62]. Regarding the contact model to use in polymer science, a debate between the JKR (Johnson, Kendall and Roberts) model [63] and the DMT (Derjaguin-Muller-Toporov) model [64] is still ongoing. Considering the low deformation target (2-4 nm) on PI and PS as well as the spherical shape of the tip, the DMT model was used in this study. Finally, it is interesting to notice that, with a contact force of 600 nN, the neat PI DMT modulus obtained by PF-QNM measurements is around 10 GPa which is close to the PI theoretical Young modulus (i.e. 8.5 GPa).

For EFM measurements, a PtIR-coated silicon tip with a resonance frequency f_0 of 66.1 kHz (determined by the auto-tune function of the Bruker multimode 8 software), a spring constant k of 2.74 N m^{-1} (determined by thermal tune) and a radius of 26 nm (determined by SEM) was used. EFM frequency shift Δf_0 measurements were done using a 50 nm lift and two different bias voltages (0 V as reference and 10 V) were applied to the AFM tip, while the sample backside was grounded. The frequency shift $a_{\Delta f}$ parameter is deduced using the following equation [65]:

$$a_{\Delta f} = \frac{\Delta f_0(V_1) - \Delta f_0(V_2)}{V_1^2 - V_2^2} \quad (1)$$

where $\Delta f_0(V_1)$ is the frequency shift measured with a bias voltage V_1 applied on the tip and $\Delta f_0(V_2)$ is the frequency shift measured with a bias voltage V_2 applied on the tip.

2.4 *EFM modeling*

To extract the relative permittivity (ε_r) cartography from frequency shift in EFM, the method developed by Riedel *et al* [65] was used. From a theoretical point of view, the frequency shift $a_{\Delta f}$ parameter is expressed by:

$$a_{\Delta f} = \frac{f_0}{4k}\frac{d^2C}{dz^2} \quad (2)$$

where d^2C / dz^2 is the second derivative of the capacitance C over the vertical position z, k is the spring constant and f_0 is the resonance frequency.

The electric field distribution in the air and in the nanodielectric layer were computed using a 2D-axisymmetric finite element model (FEM) on COMSOL Multiphysics®. Mesh was refined close to the AFM tip and the Si_3N_4 NP. Relative dielectric permittivities were fixed at $\varepsilon_{rM} = 3.5$ and $\varepsilon_{rNP} = 7.5$ for PI matrix and Si_3N_4 NP respectively. The dielectric layer was assumed to be free from electrical charges and no charge conditions (zero potential) were applied on the free boundaries of the simulation air box. These conditions ensure no edge effects. DC-bias voltage was applied on AFM tip and sample backside was grounded. The electrostatic force F_e was computed using electrostatic field E according to the following equation:

$$F_e = \frac{\varepsilon_0}{2}\iint_{tip}\|E\|^2 dS \quad (3)$$

where E is the electric field, dS the elementary surface used for the integration, ε_0 the vacuum permittivity and S the tip surface.

The capacitance second derivative was consequently deduced from the electrostatic force gradient, as:

$$\frac{d^2C}{dz^2} = 2\frac{dF_e}{dz} \quad (4)$$

By this way the frequency shift parameter $a_{\Delta f}$ could be computed, using equation 2, in various configurations: homogeneous material and nanocomposite material with or without interphase (as well as various interphase relative dielectric permittivity (ε_{rI}) values).

3. Results and discussion

3.1 Influence of Si_3N_4 silane treatment on NP dispersion

Figure 1 shows the effect of a silane coupling agent treatment of Si_3N_4 NP on the pNC surface morphology. Concerning untreated NP (figure 1(a)), the surface topography map shows a RMS roughness of 91.2 nm. The related width occurrence diagram is extracted and presents a broad distribution with an average width of 550 nm and a full width at half-maximum of 200 nm (figure 1(c)). The detected dimension is larger than the predicted one for the individual Si_3N_4 NP (approximately 20-40 nm in diameter) and could not be attributed to single NP even if the tip convolution is considered [66]. So, these broad structures are related to stacked or agglomerated NP induced by the Van der Waals inter-particle attraction between primary particles themselves. The corresponding TEM image on figure 1(c) inset shows the presence of large agglomerate as well. Concerning treated NP (figure 1(b)), the surface appears smoother and a surface RMS roughness of 21.7 nm is determined. The related width occurrence diagram is extracted and presents a sharp distribution with an average width of 250 nm and a full width at half-maximum of 50 nm as shown on figure 1(d). Indeed, the NP are highly reactive due to their relatively large surface area and small size. Their high surface energy makes them aggregate. The silane NP surface treatment decreases their surface energy and allows the NP to be better dispersed within the polymer matrix [55]. The corresponding TEM image on figure 1(d) shows a strong diminution of the agglomerate maximum size as well.

As a consequence, the affinity is an important parameter to homogeneously mix two kinds of materials. Indeed, NP aggregation leads to the deterioration of not only electrical properties, but also mechanical and thermal ones. For example, the electrical breakdown performance of polyethylene was found to be adversely affected by the presence of large aggregates of nanoclay [67]. Tensile strength and thermal conductivity were also reported to be affected by the NP agglomeration [68, 69]. Therefore, an appropriate NP dispersion within the polymer needs to be

achieved in order to ensure optimized properties of the resulting pNC. In order to disperse inorganic nano-fillers into organic polymer matrices, the affinity between their contact surfaces should be increased.

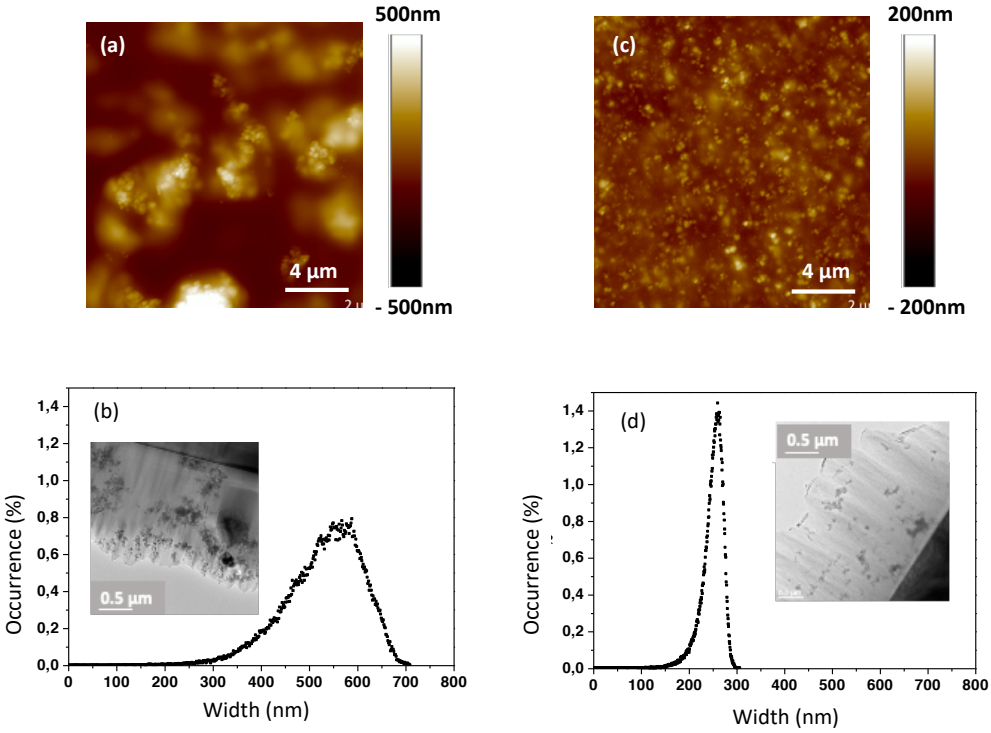

Figure 1. Nanocomposite films 20 µm × 20 µm topography map obtained in PF-QNM for (a) untreated and (c) treated Si_3N_4 NP. The related width occurrence diagram for (b) untreated and (d) treated NP. Inset the corresponding TEM images showing the NP dispersion in the PI matrix.

3.2 An optimized methodology to determine the interphase dimension by PF-QNM

In the PF-QNM mode, a lot of parameters as the contact force, the deformation or the topography could impact the results reliability concerning the mechanical properties probing. Thus, in order to accurately characterize the interphase mechanical properties, a well-controlled method is needed.

Figure 2 emphasizes the impact of the applied contact force F_c on the interphase detection. Whatever F_c is, the bump observed on topography profiles is related to the presence of the NP. For low F_c (150 nN for figure 2(a)), the Young modulus (E) is flat over the NP, which means that the force is too low to probe the NP and/or the interphase. The same behaviour is observed for all NP (i.e. whatever the bump height) showing that they are fully embedded in the matrix. When the F_c increases to medium range (600 nN for figure 2(b)), the Young modulus profile presents two zones. (i) The first one E_M, with a value around 18 GPa, is attributed to the matrix. (ii) The second one, located around the topography bump, has an apparent modulus E_I higher than the matrix one. This latter corresponds to an area where the properties of the matrix are affected by the NP presence (chains rearrangement, chemical bonds, crystallinity degree…). Consequently, this zone is attributed to the interphase. In this case, the applied force F_c is high enough to probe the interphase without reaching the NP. The interphase width (W_I) is determined as the lateral dimension of this area (in grey on figure 2(b)). The same behaviour is obtained for applied forces in the range of 200 nN to 800 nN. For high F_c (1 µN for figure 2(c)), the Young modulus profile presents two zones as well. (i) The first one with a modulus E_M around 25 GPa is related to the matrix one. (ii) The second one, at the same localization of the topography bump, with a greatly higher Young modulus and could be attributed to the NP. In this case the force is high enough to probe the NP modulus which makes the interphase dimension quite difficult to be determined.

Figure 2(d) shows the evolution of the interphase apparent Young modulus (E_I) and width W_I as a function of the applied force F_c. It can be noticed that the E_I increases continually with F_c. E_I combines both the interphase and the matrix contributions. When F_c increases, the deformation is more important and the tip probes a more important volume of the interphase. This implies the increase of E_I because the interphase Young modulus is higher than the matrix one. For low F_c values, the interphase width is low and reaches a steady state for a contact force range between 600 nN to 800 nN. This range corresponds to the contact force target allowing us to obtain a reliable interphase width measurement. In the following, an applied force of 600 nN is used.

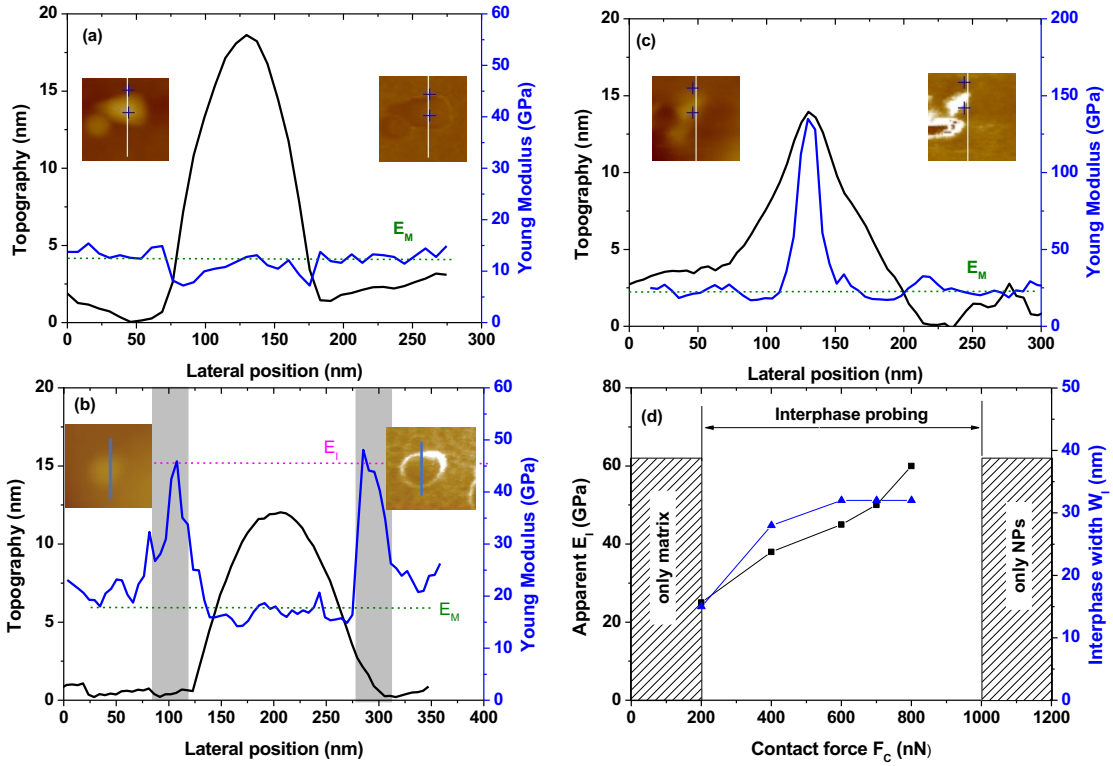

Figure 2. Topography and Young modulus profiles over an untreated NP embedded in PI obtained by PF-QNM for an applied force F_c of (a) 150 nN, (b) 600 nN and (c) 1 µN. Inset the 300 nm × 300 nm map of the topography (left) and the Young modulus (right) over the investigated NP. (d) Evolution of the interphase apparent Young modulus E_I (square) and width W_I (triangle) as a function of the applied contact force F_c.

Figures 3(a) and 3(b) present respectively the surface topography and the related Young modulus map obtained by PF-QNM for untreated NP. As previously seen, bumps on the topography map express the presence of embedded NP and their heights are related to the NP in-depth localization. On the Young modulus map, the interphase is clearly identified as a bright ring around bumps. We can highlight that the Young modulus profile is strongly affected by the bump height. Indeed, E_I increases with the bump height H as depicted on figure 3(c). This is related to the fact that the interphase area is easier to probe when the NP is protruding on the surface. Indeed, for a fixed F_c and surface deformation, the probed interphase volume is higher when the NP is protruding over the surface. This is the reason behind the E_I increase with the bump height, whereas the bump height has a low impact on the interphase width determination (figure 3(c)). A W_I value of 33 ± 2 nm is obtained in the case of untreated NP. Figures 3(d) and 3(e) present respectively the surface topography and the related Young modulus map obtained by PF-QNM for treated NP. As previously, embedded NP could be identified as a bump on the topography map. However, the interphase is less visible on the Young modulus map. This implies that the interphase modulus E_I increase with the bump height H is lower than for untreated NP (figure 3(f)). Moreover, for treated NP, the interphase width W_I appears to be quite independent of the bump height and has a value of around 42 ± 3 nm.

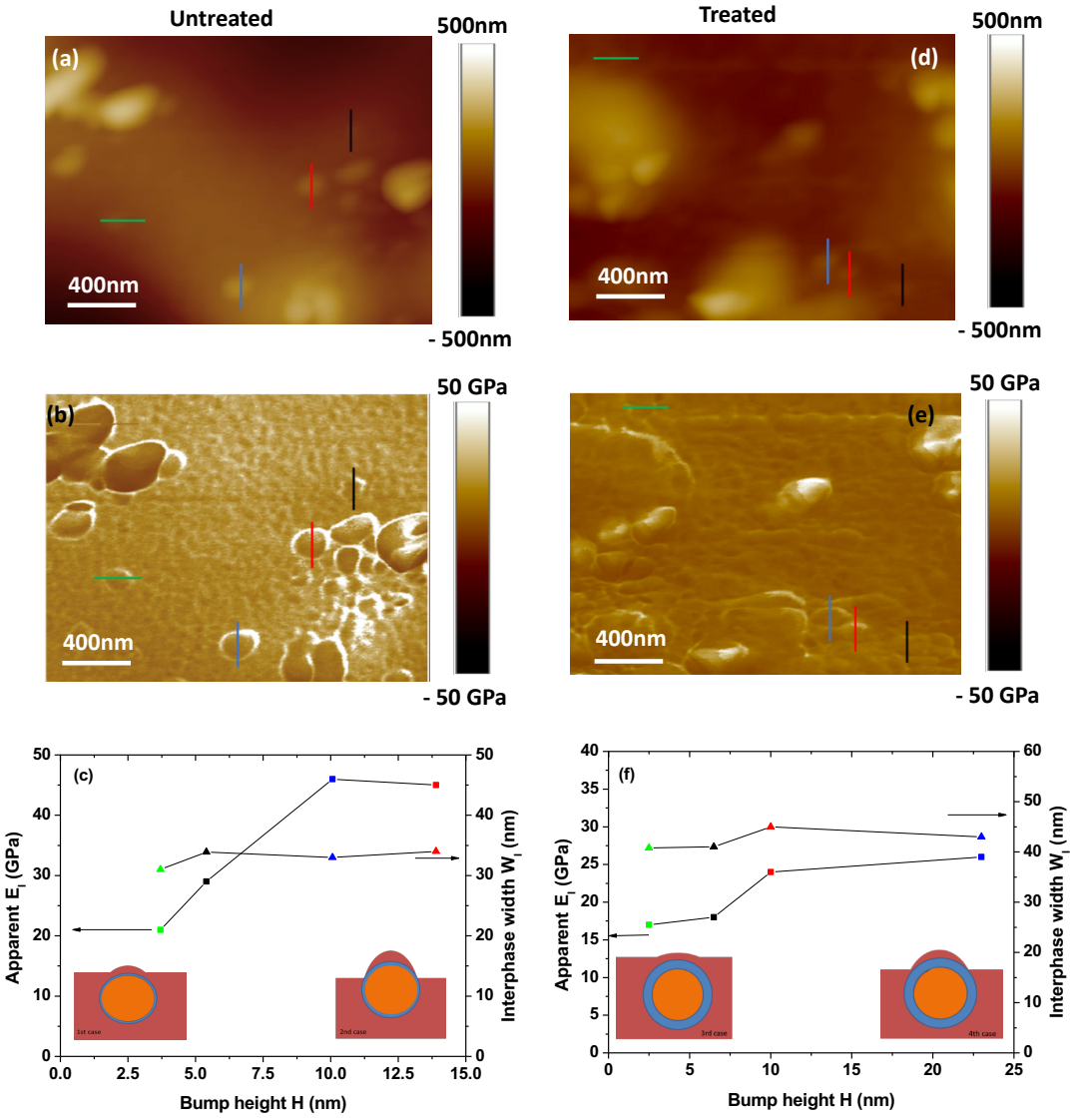

Figure 3. (a, d) Topography and (b, e) Young modulus maps obtained by PF-QNM on (a, b) untreated and (d, e) treated PI/Si_3N_4 pNC (F_c = 600 nN). Evolution of the interphase apparent Young modulus E_I (square) and width W_I (triangle) as function of the bump height H (symbol colors correspond to the localization on topography and Young modulus maps) for (d) untreated and (f) treated PI/Si_3N_4 nanocomposite.

From the methodology point of view, it is clear that the interphase properties measurement is more accurate for middle range contact force values (600 nN < F_c < 800 nN) and for protuberant particles where the interphase is more exposed to the surface. Moreover, W_I values are equal to 33 ± 2 nm and 42 ± 3 nm for untreated and treated NP respectively. The interphase thickness measurement error is low (< 8.8 %) for all samples and seems to be independent of the particles topography profile (protuberant or immersed NP).

Table 1 shows a comparison between our results and previous studies available in the literature for various pNC. Whatever the pNC, the interphase region exhibits a higher elastic modulus compared to the matrix. This indicates that polymer chains present a better organization at the interphase or a restricted movement due to the NP presence. Moreover, the interphase thicknesses reported in this study are in agreement with the interphase models prediction [25, 26] and other pNC interphase measurements at the nanoscale [36, 38, 39, 70, 71] or macroscale [72] reported

in the literature. Finally, the interphase thickness is higher for treated NP. Indeed, the silane coupling agent allows the particles to better interact with the surrounding polymer chains [21, 55].

Table 1. Comparison of interphase thicknesses W_I and Young moduli E_I for various pNC.

Matrix	**Nanofiller**	**Method**	W_I **(nm)**	E_I **(GPa)**	**Ref.**
PI	untreated Si_3N_4 NP	PF-QNM case of figure 2(b)	33 ± 2	> E_{matrix}	This study
Polyvinyl alcohol	nanobamboo charcoals	PF-QNM case of figure 2(c)	13–16	20–70 (> 24 for PVA)	[38]
	cellulose nanocrystals	PF-QNM case of figure 2(c)	11–13	/	[36]
Hydrogeneted nitrilebutadiene rubber (HNBR)	carbon black	AFM torsional harmonix	19 ± 8	53 (> 4 for HNBR)	[71]
Epoxy	graphen oxyde / graphen nanoplatelets	STEM / EELS	12.5–13	/	[70]
	$BaTiO_3$	EFM (profile width)	25	/	[39]
	Al_2O_3	pNC Young modulus combined with model	36	40 > E_{matrix}	[72]
	TiO_2		19	22 > E_{matrix}	

3.3 Nanoscale dielectric characterization

Figure 4 summarizes EFM measurements performed on pNC samples. Topography map emphasizes isolated NP (addressed by arrows) close to the surface for samples without (figure 4(a)) and with (figure 4(d)) silane treatment. Following the methodology described in part 2.4, the frequency shift parameter $a_{\Delta f}$ obtained using equation 1 is presented in figures 4(b) and 4(e). Apparent ε_r maps (figures 4(c) and 4(f)) are deduced from $a_{\Delta f}$ using COMSOL model, which considers the pNC layer as a homogeneous material. Results show that, whatever the surface treatment is, ε_r is lower on the NP. Indeed, ε_r is around 2.9-3 in the NP area and around 3.35 for the matrix, which is close to the theoretical value for PI. Moreover, the ε_r over silane-treated NP seems to be a little bit lower than the one over non-treated NP. This effect could be related to both W_I and ε_{rI}. Indeed, because ε_{rI} is lower than ε_{rM} and because W_I is higher for the treated NP, the application of laws such as the simple mixing law or the interphase powel law [27] predicts a lower value of the apparent ε_r for treated NP compared to untreated NP.

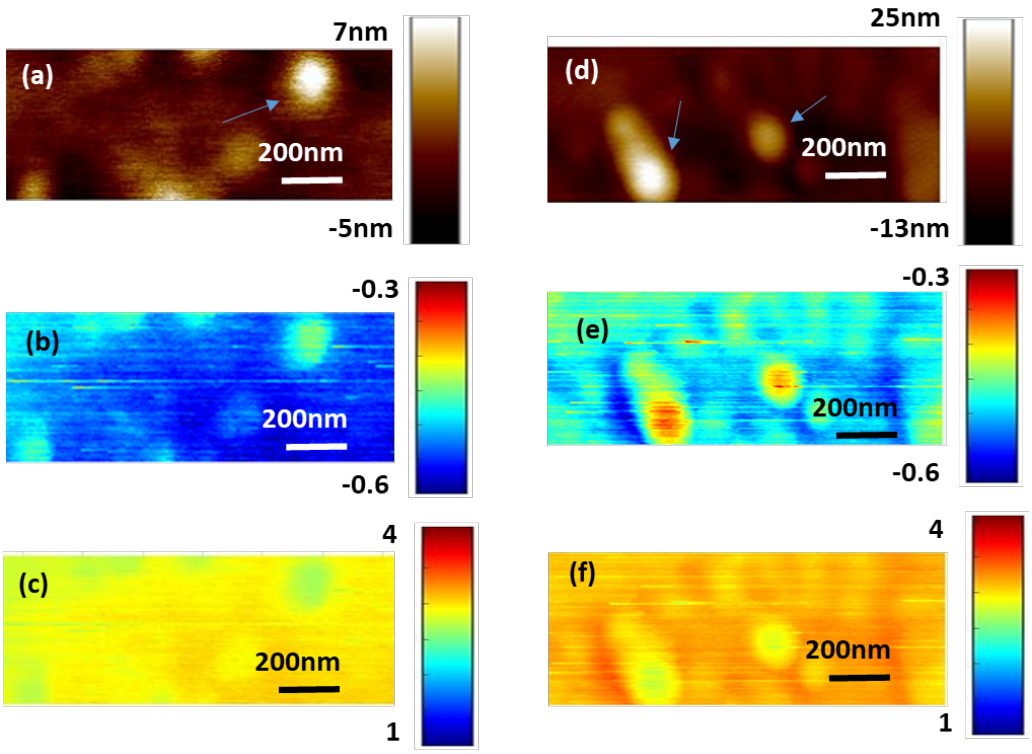

Figure 4. EFM maps for pNC without (a-c) and with (d-f) silane treatment for Si_3N_4 NP. (a, d) Surface topography, (b, e) frequency shift parameter $a_{\Delta f}$ and (c, f) apparent relative dielectric permittivity.

As ε_r of Si_3N_4 NP is higher than PI, the application of the simple mixing law fails to explain the decrease of the apparent ε_r over the NP. This decrease could be related either to the electrostatic screening effect as for metallic NP based NC [73] or to the presence of an interphase area [27]. To investigate the screening effect hypothesis, a FEM model representing the real sample geometry is proposed. This is composed of a PI matrix ($\varepsilon_{rM} = 3.5$) and a 20 nm-radius Si_3N_4 NP ($\varepsilon_{rNP} = 7.5$). The resulting electric field distribution is represented on figure 5(a). Figure 5(b) shows the apparent ε_r evolution over the NP as a function of the distance between the NP and the pNC surface. Results emphasize that the dielectric permittivity increases when the NP is close to the surface. Therefore, the decrease of the apparent ε_r over the NP is not related to an electrostatic screening effect due to the presence of the Si_3N_4 NP. Consequently, a more complex FEM model taking into account the presence of the interphase is proposed and the electrical field distribution is computed (figure 5(c)). Figure 5(d) represents the evolution of the computed frequency shift parameter $a_{\Delta f}$ as a function of the interphase relative dielectric permittivity for different interphase thicknesses. Results highlight that all curves intercept at $a_{\Delta f} = -0.53$ Hz / V² and $\varepsilon_r = 3.5$, which corresponds to the PI matrix parameters. When the interphase permittivity is lower than the matrix one, an increase of the interphase thickness induces an increase of the frequency shift parameter as well. Whereas when the interphase permittivity is higher than the matrix one, an increase of the interphase thickness induces a decrease of the frequency shift parameter. Moreover, the $a_{\Delta f}$ variation in function of ε_{rI} shows a steeper slop for higher W_I values. This shows a higher sensitivity between the $a_{\Delta f}$ and the ε_{rI} determination when the interphase width is more important. This behaviour was already observed in a modeling study concerning a pNC (with $\varepsilon_M = 4$, $\varepsilon_{NP} = 10$ and a NP radius of 25-50 nm) [42]. Finally, as shown in figure 5(d), when the interphase thickness increases a characteristic behaviour tending to a homogeneous material one is observed. In fact, when W_I reaches higher values than the NP radius and/or the pNC thickness (i.e. tends to infinity), the pNC becomes mainly composed of the interphase.

Therefore, according to figure 5(d), we can identify that an interphase with a lower permittivity than the matrix one is needed to explain experimental results presented in figure 4. This interphase lower permittivity compared to the matrix is in total agreement with its higher elastic modulus measured by PF-QNM and confirms a better polymer

chain organization and a restricted chain mobility within the interphase area. In the following, interphase properties (thickness and dielectric permittivity) will be determined using this model.

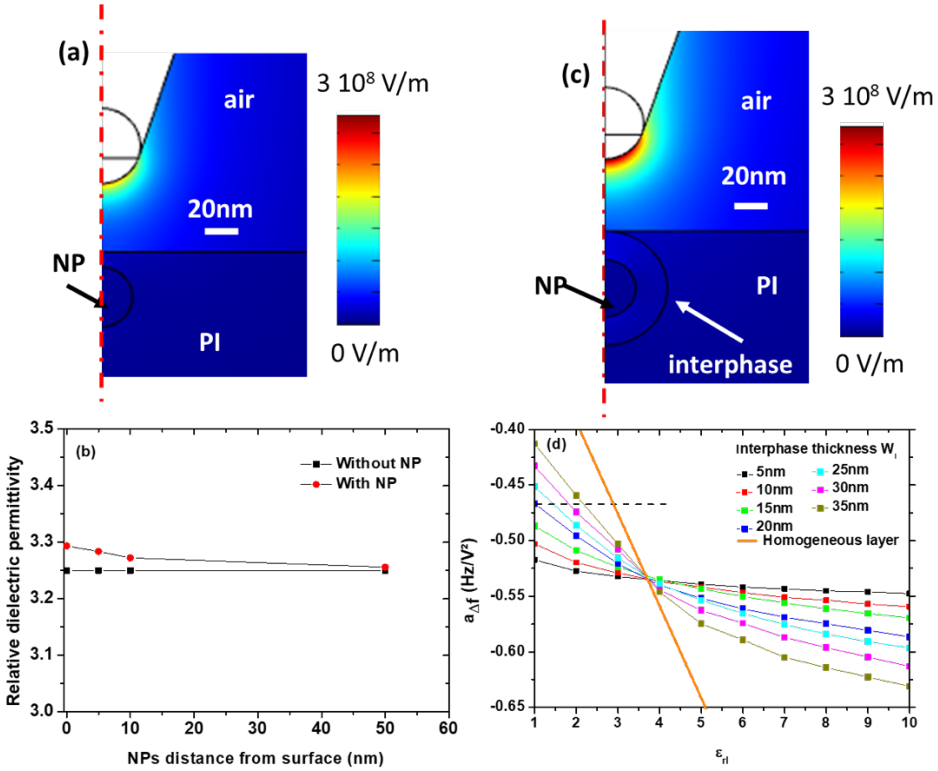

Figure 5. (a) Electric field computed in air and in pNC film for a Si_3N_4 NP localized at 5 nm from the surface. (b) Evolution of the apparent ε_r computed for different distances between the NP and the surface. (c) Electric field computed in air and in pNC film for a Si_3N_4 NP surrounded by an interphase ($W_I = 20$ nm and $\varepsilon_{rI} = 2$). (d) Evolution of the frequency shift parameter $a_{\Delta f}$ as function of ε_{rI} for different interphase thicknesses W_I. In all models, NP presents a radius of 20 nm, pNC film is 2.3 µm-thick which corresponds to the pNC without treatment and 10 V is applied on the AFM tip.

3.4 *Discussion on the interphase morphological and dielectric properties*

In this section, the methodology used to measure the interphase properties is described showing how mechanical and dielectric local measurements are complementary for the interphase characterization.

We have focused our interest on a protuberant NP and more particularly on a 10 nm-heigth one for both untreated and treated NP. Figure 6(a) compares topography and $a_{\Delta f}$ profiles over a NP without treatment. $a_{\Delta f}$ is equal to - 0.53 Hz / V² over the matrix and -0.47 Hz / V² over the NP. The same behaviour is observed for NP with silane treatment with an $a_{\Delta f}$ equal to - 0.47 Hz / V² over the matrix and - 0.39 Hz / V² over NP.

According to figure 5(d), a lot of ε_{rI} / W_I couples are possible to describe the interphase for untreated NP. Indeed, the interphase thickness needs to be higher than 20 nm and its ε_{rI} should be between 1 and 3. Consequently, with only EFM results it is only possible to conclude that the interphase permittivity is lower than the matrix one.

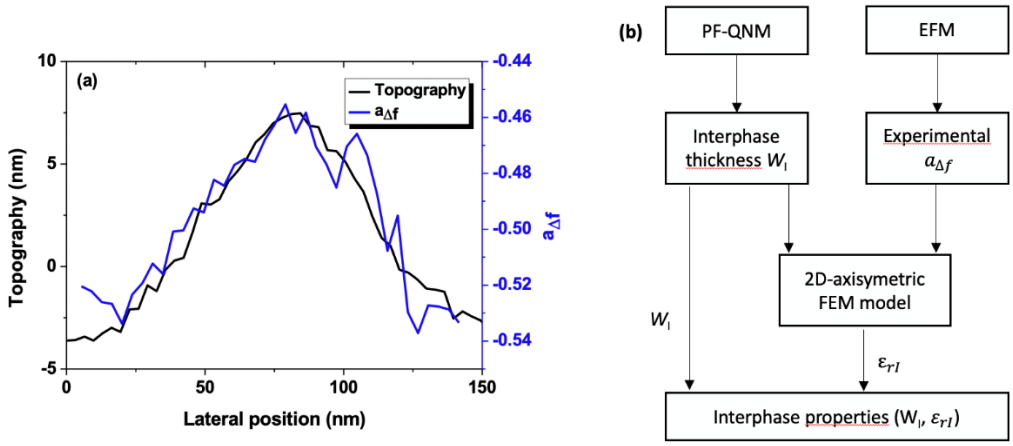

Figure 6. (a) Comparison of topography and $a_{\Delta f}$ profiles over Si_3N_4 NP without silane treatment. (b) The interphase characterization process.

Therefore, to characterize the interphase properties at the nanoscale a two steps process is proposed (figure 6(b)). (i) The first step consists of mechanical properties characterization using PF-QNM to determine the interphase width W_I. It is important to choose a protuberant NP to insure that both the interphase and the NP are close to the surface. (ii) The interphase relative dielectric permittivity is determined using the modified 2D-axisymetric FEM model (figure 5(c)) including the Si_3N_4 NP (radius 10-40 nm) and the interphase (W_I values close to those obtained from experimental measurements: 30 nm and 40 nm for untreated and treated NP respectively). The only remaining unknown parameter is ε_{rI}. This parameter is adjusted to fit with the experimental $a_{\Delta f}$ value obtained over the NP. So, combining PF-QNM and EFM permits to characterize the interphase dimension and relative dielectric permittivity.

Table 2 summarizes results obtained with the above methodology for both untreated and treated NP. The NP radius and interphase thickness dispersion are taken into account and present a great impact on ε_{rI} .The ε_{rI} values are similar for untreated and treated NP and are lower than the matrix ε_r. This behaviour was extensively predicted in previous studies at macroscale by combining modeling and dielectric spectroscopy for various pNC as LDPE/Al_2O_3 [32], epoxy/Al_2O_3 [74], and more rarely at nanoscale using EFM as for PE/TiO_2 pNC [43]. However, whatever the scale approach, the interphase thickness remained generally unknown and hypotheses were done to predict ε_{rI}. In rare cases, as for epoxy/$BaTiO_3$ pNC, a ε_{rI} higher than the matrix ε_r was found [39, 44].

Table 2. Interphase thickness W_I and relative permittivity ε_{rI} as a function of NP treatment

NP radius	**Untreated**		**Treated**	
	W_I	ε_{rI}	W_I	ε_{rI}
10 nm	30 nm ± 2 nm	1.8 ± 0.4	40 nm ± 3 nm	1.9 ± 0.3
20 nm		1.5 ± 0.5		1.7 ± 0.4
30 nm		1.3 ± 0.4		1.6 ± 0.3
40 nm		1.2 ± 0.4		1.5 ± 0.3

Our results on PI/Si_3N_4 pNC have shown that the interphase presents higher Young modulus and lower relative dielectric permittivity than the PI matrix. These results are in agreement with an interphase area where the polymer chains are better organized around the NP playing the role of a nucleation agent [75]. Indeed, previous studies have shown that the chains organisation induces the Young modulus increase [76] and the dielectric permittivity decrease [77] in polymer materials. Moreover, a study dealing with the charge injection and transport in the interphase area has shown a higher conductivity close to the NP compared to PI [78]. This is also in agreement with the better chains organization.

Figure 7 illustrates our phenomenological model to describe the interphase for untreated and treated NP (figure not on scale). Concerning untreated NP, the interphase is composed only by a well-organized polymer chains. However, for treated NP another layer, related to the silane treatment, should be taken into consideration [55, 56, 79]. Besides, our results emphasize that ε_{rI} is quite the same for both treated and untreated NP (Table 2). So, the layer related to the silane treatment have a weak influence on ε_{rI} probably due to its low thickness predicted to be around few atoms thick [79].

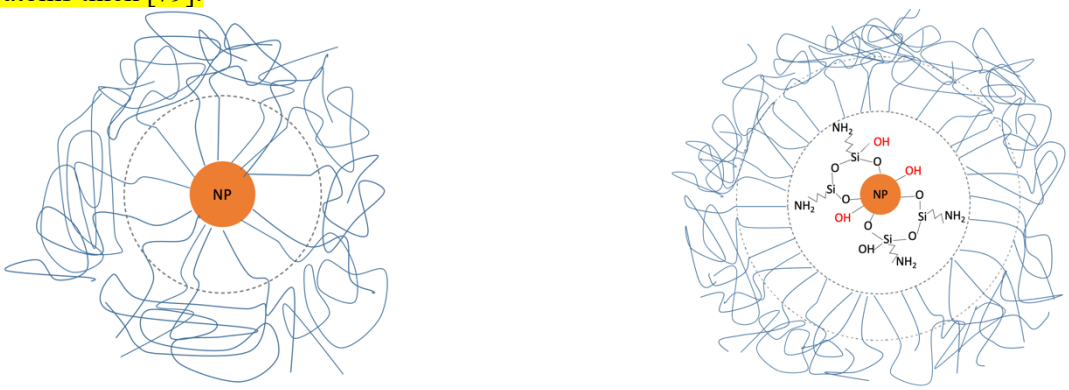

(a) (b)

Figure 7. Illustration of the model proposal for NP/polymer interphase zone for (a) untreated and (b) treated NP (figure not on scale).

4. Conclusion

In this study, the PF-QNM and EFM modes were applied to directly probe the mechanical and dielectric properties of PI/Si_3N_4 NC with a particular focus on the interphase region for untreated and silane treated particles. A first attention was given to the study of NP dispersion within the host matrix in both cases. Results show a better dispersion of treated Si_3N_4 within the PI matrix compared to untreated particles.

This work has presented in detail a new approach to quantitatively measure the interphase thickness and properties. Experimental results indicate that the interphase area have a higher Young modulus and a lower permittivity than the matrix (1.5-1.9 depending on the NP radius). Thus, the interphase represents an organized polymer chain area around the NP where the chain mobility is restricted. Moreover, the particle surface silane treatment has an effect on the interphase thickness increase (from 32 nm to 42 nm) but do not influence its dielectric properties. Finally, a phenomenological model was given in order to describe the interphase behaviour within pNC materials.

Understanding the interphase area properties at the nanoscale may be the key process to explain the improvements observed for pNC electrical properties at the macroscopic scale. Moreover, these results could have a great impact on pNC dielectric properties modeling as they constitue accurate imput physical parameters.

References

[1] Diaham S, Locatelli M.-L, and Khazaka R 2012 BPDA-PDA Polyimide: Synthesis, Characterizations, Aging and Semiconductor Device Passivation in *High Performance Polymers* (InTechOpen publishing)
[2] Barré O and Napame B 2017 *Machines* **5** 7
[3] Delpino S, Fabiani D, Montanari G.C, Laurent C, Teyssedre G, Morshuis P.H.F, Bodega R and Dissado L.A 2008 *IEEE Electr. Insul. Mag.* **24** 14
[4] Ghosh D and Khastgir D 2018 *ACS Omega* **3** 11317
[5] Lewis T.J 1994 *IEEE Trans. Dielectr. Electr. Insul.* **1** 812
[6] Lau K.Y and Piah A.M 2011 *Malays. Polym. J.* 6 58
[7] Gao Y, Picot O T, Bilotti E and Peijs T 2017 *Europ. Polym. J.* **86** 117

[8] Paramane A.S and Kumar K.S 2016 *Trans. Electr. Electron. Mat.* **17** 239
[9] Plesa I, Notingher P.V, Schlogl S, Sumereder C and Muhr M 2016 *Polymers* **8** 173
[10] Adnan M.M, Dalod A.R.M, Balci M.H, Glaum J and Einarsrud M.A 2018 *Polymers* **10**, 1129
[11] Li Q *et al* 2015 *Nature* **523** 576
[12] Nelson J.K and Fothergill J 2004 *Nanotechnology* **15** 586
[13] Tanaka T, Montanari G.C and Mulhaupt R 2004 *IEEE Trans. Dielectr. Electr. Insul.* **11** 763
[14] Guadano L, Naddeo C, Raimondo M, Barra G, Vertuccio L, Russo S, Lafdi K, Tucci V, Spinelli G and Lamberti P 2017 *Nanotechnology* **28** 094001
[15] Karak N 2019 *Nanomaterials and Polymer Nanocomposites: Raw Materials to Applications* (India: Elsevier)
[16] Milliere L, Makasheva K, Laurent C, Despax B and Teyssedre G 2014 *Appl. Phys. Lett.* **105** 122908
[17] Diaham S, Saysouk F, Locatelli M.-L and Lebey T 2015 *J. Phys. D: Appl. Phys.* **48** 385301
[18] Diaham S, Pizzutilo E and Locatelli M.-L 2016 *Proc. IEEE Inter. Conf. Dielectr.* **1** 72
[19] Sadasivuni K.K, Ponnamma D, Kim J and Sabu T 2015 *Graphene-Based Polymer Nanocomposites in Electronics* (Switzerland: Springer International Publishing)
[20] Bikiaris D 2010 *Materials* **3** 2884
[21] Luo H, Zhou X, Ellingford C, Zhang Y, Chen S, Zhou K, Zhang D, Browen C.R and Wan C 2019 *Chem. Soc. Rev.* **48** 4424
[22] Pandey J.C and Singh M 2020 *Polymer Testing* **91** 106802
[23] Chen J, Wang X, Yu X, Yao L, Duan Z, Fan Y, Jiang Y, Zhou Y and Pan Z 2018 *J. Mater. Chem. C* **6** 271
[24] Li Z, Okamoto K, Ohki Y and Tanaka T 2011 *IEEE Trans. Dielectr. Electr. Insul.* **18** 675
[25] Tanaka T, Kosako M, Fuse N and Ohki Y 2005 *IEEE Trans. Dielect. Electr. Insul.* **12** 669
[26] Raetzke S and Kindersberger J 2010 *IEEE Trans. Dielectr. Electr. Insul.* **17** 607
[27] Todd M.G and Shii F.G 2005 *IEEE Trans. Dielectr. Electr. Insul.* **12** 601
[28] Lewis T.J 2004 *IEEE Trans. Dielectr. Electr. Insul.* **11** 739
[29] Wang Z, Lv Q, Chen S, Li C, Sun S and Hu S 2016 *ACS Appl. Mater. Interfaces* **8** 7499
[30] Maity P, Gupta N, Parameswaran V and Basu S 2010 *IEEE Trans. Dielectr. Electr. Insul.* **17** 1665
[31] Pandey J.C and Gupta N 2016 *IEEE Trans. Dielectr. Electr. Insul.* **23** 2747
[32] Wang W and Li S 2018 *IEEE Trans. Dielectr. Electr. Insul.* **25** 2
[33] Wang D, Fujinami S, Nakajima K, Niihara K, Inukai S, Ueki H, Magario A, Noguchi T, Endo M and Nishi T 2010 *Carbon* **48** 3708
[34] Frechette M, Preda I, Veilette R and Moraille P 2014 *Proc. IEEE Electr. Insul. Conf. IEC* 312
[35] Qu M, Deng F, Kalkhoran S.M, Gouldstone A, Robisson A and Van Vliet K.J 2011 *Soft Matter* **7** 1066–1077
[36] Pakzad A, Simonsen J and Yassar R.S 2012 *Compos. Sci. Tech.* **72** 314
[37] Houssat M, Lahoud Dignat N, Cambronne J.-P and Diaham S 2018 *IEEE Trans. Nanotech.* **17** 1146
[38] Moussa M and Dong Y 2018 *Nanotechnology* **29** 385701
[39] Sharma A, Basu S. and Gupta N 2020 *IEEE Trans. Dielectr. Electr. Insul.* **27** 433
[40] El Khoury D, Fedorenko V, Castellon J, Bechelany M, Laurentie J.-C, Balme S, Fréchette M, Ramonda M and Arinero R 2017 *Scanning* 4198519
[41] Gupta P, Schadler L.S and Sundararaman R 2021 *Materials Characterization* **173** 110909
[42] El Khoury D, Arinero R, Laurentie J.-C, Bechelany M, Ramonda M and Castellon J 2018 *Beilstein J. Nanotechnology* **9** 2999
[43] Peng S, Zeng Q, Yang X, Hu J and He J 2016 *Scientific reports* **6** 38978
[44] Sharma A, Basu S and Gupta N 2020 *IEEE Trans. Dielectr. Electr. Insul.* **27** 866
[45] Borgani R, Pallon L.K, Hedenqvist M.S, Gedde U.W and Haviland D.B 2016 *Nano Lett.* **16** 5934
[46] Peng S, Luo Z, Wang S, Liang J, Yuan C, Yuan Z, Hu J, He Jand Li Q 2020 *ACS Appli. Mater. Interfaces* **12** 53425
[47] Peng S, Yang X, Yang Y, Wang S, Zhou Y, Hu J, Li Q and He J 2019 *Adv. Mater.* 1807722
[48] Ghosh M.K and Mittal K.L 1996 *Polyimides: fundamentals and applications* (Boca Raton: CRC press)
[49] Ai D, Li H, Zhou Y, Ren L, Han Z, Yao B, Zhou W, Zhao L, Xu J and Wang Q 2020 *Adv Energy Mater* **10** 1903881
[50] Diaham S, Locatelli M.-L and Lebey T 2007 *Appl. Phys. Lett.* **91** 122913
[51] Miyairi K 2001 *Japanese J. Appl. Phys. Part 1* **40** 3A 1297-1299
[52] Hassan Y.A. and Hu H 2020 *Composites Part A* **138** 106064
[53] Chen M. , Zhou W., Zhang J. and Chen Q. 2020 *Polymers* **12** 322
[54] Diaham S, Saysouk F, Locatelli M.-L and Lebey T 2016 *IEEE Trans. Dielectr. Electr. Insul.* **23** 5 2795-2803

[55] Tawade B.V, Apata I.E, Singh M, Das P, Pradhan N, Al-Enizi A.M , Karim A and Raghavan D 2021 *Nanotechnology* **32** 142004
[56] Yang X, Jiang Z, Li W, Wang C, Chen M and Zhang G 2020 *Nanotechnology* **31** 275710
[57] Young T.J, Monclus M.A, Burnett T.L, Broughton W.R, Ogin S.L and Smith P.A 2011 *Meas. Sci. Technol.* **22** 125703
[58] Pittenger B, Erina N, Su C 2012 *Quantitative Mechanical Property Mapping at Nanoscale with PeakForce QNM* Bruker Application Notes 128
[59] Houssat M, Lahoud Dignat N, Villeneuve-Faure C, Cambronne J.-P 2018 *IEEE 13th Nanotechnology Materials and Devices Conference (NMDC)*
[60] Sader J.E, ChonJ.W.M and Mulvaney P 1999 *Rev. Scientif. Instrum.* **70** 3967
[61] Dokukin M.E and Sokolov I 2012 *Langmuir* **28** 16060
[62] Dokukin M.E and Sokolov I 2012 *Macromolecules* **45** 4277
[63] Johnson K.L, Kendall K and Roberts A.D 1971 *Proc. R. Soc. A Math. Phys. Eng. Sci.* **324** 1558
[64] Derjaguin B.V, Muller V.M, and Toporov Y.P 1975 *J. Colloid Interface Sci*. **53** 2 314-326
[65] Riedel C, Arinero R, Tordjeman Ph, Leveque G, Swartz G.A, Alegria A and Colmenero J 2010 *Phys. Rev. B* **81** 010801
[66] Sawyer L.C, Grubb D.T and Meyers G.F 2008 *Polymer Microscopy* (New York: Springer)
[67] Vaughan A.S, Swingler S.G, and Zhang Y 2006 *IEEJ Trans. Fundam. Mater.* **126** 1057-1063
[68] Wernik J.M and Meguid S.A 2014 *Mater. Des.* **59** 19-32
[69] Ashraf M.A, Peng W, Zare Y and Rhee K.Y 2018 *Nanoscale Res Lett.* **13** 214
[70] Liu Y, Hamon A.L, Haghi-Ashtiani P, Reiss T, Fan B, He D and Bai J 2016 *ACS Appl. Mater. Interf.* **8** 34151
[71] Qu M, Deng F, Kalkhoran S.M, Gouldstone A, Robison A and Van Vliet K.J 2011 *Soft Matter.* **7** 1066
[72] Deng F and Van Vliet K.J 2011 *Nanotechnology* **22** 165703
[73] Villeneuve-Faure C, Makasheva K, Djaou C, Boudou L and Teyssedre G 2018 *Proc. IEEE 13th Nanotechnology Materials and Devices Conference (NMDC)* (10.1109/NMDC.2018.8605887)
[74] Maity P, Gupta N, Parameswaran V and Basu S 2010 *IEEE Trans. Dielectr. Electr. Insul.***17** 1665
[75] Pourrahimi M, Hoang T.A, Liu D, Pallon L.K, Gubanski S, Olsson R.T, Gedde U.W and Hedenqvist M.S 2016 *Adv. Mater*. **28** 8651
[76] Aliotta L, Gazzano M, Lazzeri A and Righetti M.C 2020 *ACS Omega* **33**, 20890
[77] Zakiyan E.E, Azizi H and Ghasemi I 2017 *Composites Science and Technology* **142**, 10
[78] Houssat M, Villeneuve-Faure C, Lahoud Dignat N and Cambronne J.P 2020 *Proc. IEEE 3rd International Conference on Dielectrics (ICD)* (10.1109/ICD46958.2020.9341839)
[79] Alhabill F.N, Ayoob R, Andritsch T and Vaughan A.S. 2018 *Materials and Design* **158** 62